Building Ultrathin $Li_4Mn_5O_{12}$ Shell for Enhancing the Stability of Cobalt-Free Lithium-Rich Manganese Cathode Materials

Yuhong Qiu [1,2], Xuefeng Peng [1], Lichun Zhou [2], Jie Yan [1], Yaochen Song [1,2], Linnan Bi [1,2], Xin Long [1,2], Liang He [2], Qingyu Xie [2], Sizhe Wang [2,3,*] and Jiaxuan Liao [1,2,*]

1 School of Materials and Energy, University of Electronic Science and Technology of China, Chengdu 611731, China
2 Yangtze Delta Region Institute (QuZhou), University of Electronic Science and Technology of China, Quzhou 324000, China
3 School of Materials Science and Engineering, Shaanxi Key Laboratory of Green Preparation and Functionalization for Inorganic Materials, Shaanxi University of Science & Technology, Xi'an 710021, China
* Correspondence: kevinwang@sust.edu.cn (S.W.); jxliao@uestc.edu.cn (J.L.)

Abstract: Spinel $Li_4Mn_5O_{12}$ was successfully prepared by the wet chemical method to modify the surface of $Li_{1.2}Ni_{0.2}Mn_{0.6}O_2$. The results showed that an ultrathin spinel $Li_4Mn_5O_{12}$ surface-modified layer with a thickness of approximately 10 nm was successfully constructed on the raw material surface, and that the cationic order was improved. In addition, the lithium ion diffusion coefficients (D_{Li}^+) of the raw materials and the modified materials were calculated using the EIS test and impedance fitting. The results indicated that the ultrathin $Li_4Mn_5O_{12}$ surface modification shell can increase the lithium ion diffusion rate of the material and improve the rate capability of the material. So, the surface modification layer of spinel $Li_4Mn_5O_{12}$ can reduce the oxygen loss of the first cycle and improve the cationic order of the material. Therefore, the first coulombic efficiency of $Li_4Mn_5O_{12}/Li_{1.2}Ni_{0.2}Mn_{0.6}O_2$ material at the current density of 12.5 mA·g^{-1} reaches 80.46%, and the capacity retention rate reaches 91.74% after 50 cycles, which are 3.36% and 21.23% higher than those of the raw materials, respectively. It showed better electrochemical reversibility and cyclic stability. This study provides a straightforward and convenient modification method for improving the stability of cobalt-free lithium-rich manganese cathode materials and has a favorable application prospect.

Keywords: lithium-ion battery; positive electrode; cobalt-free lithium-rich manganese oxide; $Li_4Mn_5O_{12}$-coated

1. Introduction

The lithium-ion battery is an ideal energy storage device with the advantages of high energy density, long service life, and good safety performance [1–6]. However, as an energy storage device, the lithium-ion battery still has room for improvement in terms of energy density and cost [7–10]. At the end of the last century, $LiCoO_2$, $LiMn_2O_4$ and $LiFePO_4$ were discovered and successfully applied to lithium-ion batteries, which have become the cathode materials of lithium-ion batteries commercialized at present [6,11–14]. However, the current discharge-specific capacity of positive electrode materials is not up to 200 mAh·g^{-1}, whereas the reversible specific capacity of commercial negative electrode materials is more than 350 mAh·g^{-1}. In addition, the cost of positive materials in a single cell is much higher than the cost of negative materials. Therefore, the energy density and cost of current lithium-ion batteries are mainly limited by the cathode material. Therefore, it is of great significance to research and develop cathode materials with high energy density and low cost [8,15–17].
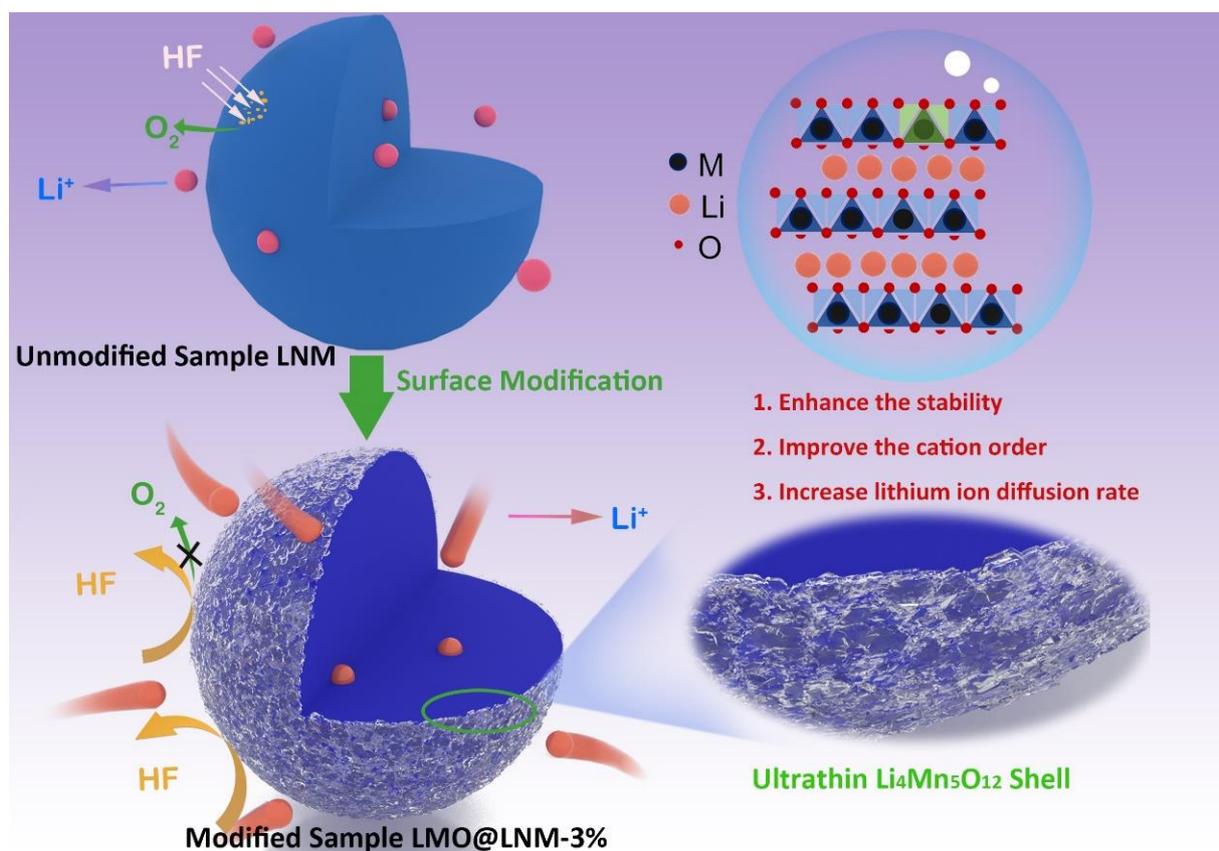
In recent years, ternary materials ($LiNi_xCo_yMn_{(1-x-y)}O_2$) and Li-rich manganese cathode materials ($xLi_2MnO_3·(1-x)LiMO_2$; M is at least one of the transition metals)

have attracted people's attention [18–20]. The cobalt-free lithium-rich manganese cathode material is an ideal cathode material with a high discharge specific capacity ($\geq 250 \, \text{mAh} \cdot \text{g}^{-1}$) and relatively low preparation cost [21,22]. However, during the charge–discharge cycles, a variety of transitional metal cations and oxygen ions occurred. These reactions have caused problems such as poor circulation performance, fast voltage attenuation, poor performance, and low first coulombic efficiency, which limits its actual application [23].

In order to alleviate problems such as oxygen loss and transition metal migration, researchers have proposed a variety of solutions, such as ion doping, surface modification, etc. [24–27]. Generally, doping ions have a large ion radius, which can reduce the dynamic migration of transition metal ions by increasing the migration barrier [23]. Moreover, due to the electrochemical inertness of the doped elements, the stability of the structure can be maintained. Therefore, ion phase doping can optimize the structure of the material, thereby improving the electrochemical properties of the material. Li et al. inhibited the formation of lithium vacancies and the migration of manganese ions by doping K^+ in the bulk phase of lithium-rich materials [28]. In addition, reducing the oxygen release in the material lattice can also inhibit the migration and phase transition of transition metal ions, thus reducing the voltage drop and improving the cycle stability. Surface coating is an effective means of relieving oxygen release. Wu et al. systematically studied various oxide coatings (Al_2O_3, CeO_2, ZrO_2, SiO_2, ZnO) and demonstrated that they can retain oxygen vacancies and improve cycle stability [29]. Liu et al. directly coated LiF on $Li_{1.2}Ni_{0.15}Fe_{0.1}Mn_{0.55}O_2$ surface by the high-temperature melting method, which improved the cyclic stability of the material [30]. The active material coated with 0.5 wt.% LiF has a discharge capacity approaching 199 $\text{mAh} \cdot \text{g}^{-1}$ after 100 cycles. Chen et al. used organic fluorine and spinel $Li_{1+x}Ni_yMn_{2-y}O_4$ coating for fluorine doping to improve the electrochemical performance of the material by increasing the diffusion rate of Li^+ ions [31]. The discharge capacity of the modified sample reached 256.1 mAh g^{-1} at 0.5 C, and could still reach 112.6 mAh g^{-1} at 10 C. Zhao et al., using a simple eutectic molten-salt method, in the lithium cathode $Li_{1.2}Ni_{0.13}Fe_{0.13}Mn_{0.54}O_2$, built in functional coating and doping [32]. After 120 cycles at 0.2 C, the material still retained 90.1% of its initial capacity.

Spinel $Li_4Mn_5O_{12}$ is a high-power lithium-ion battery cathode material due to its high lithium-ion conductivity and electrochemical stability. In addition, the spinel $Li_4Mn_5O_{12}$ has half of the octagonal space point, and therefore it can be used as a lithium storage carrier to reinsert irreversible lithium ions in the lithium-rich materials during the first cycle. Therefore, spinel $Li_4Mn_5O_{12}$ can not only be used as a good cathode material for lithium-ion batteries, but also as a high-performance coating of lithium-rich composite materials [33].

In this study, a simple method for modifying cobalt-free lithium-rich manganese-based cathode materials by spinel $Li_4Mn_5O_{12}$ surface modification was proposed. Through the method of wet chemistry, the $Li_{1.2}Ni_{0.2}Mn_{0.6}O_2$ material prepared using the solution–gel method will be mixed with the appropriate amount of metal salt solution. Then, after the mixture has reacted in a constant-temperature water bath and calcined at an appropriate temperature, a spinel/layered heterostructure layer is constructed on the surface of active material particles. At the same time, the influence of the modified layer on the size of the primary particle, on the surface morphology of the secondary particle, the crystal structure, and the electrochemical performance of the active material was studied. As depicted in Figure 1, the surface modification layer of spinel $Li_4Mn_5O_{12}$ can improve the cationic order and the lithium ion diffusion rate of the raw materials.

Figure 1. Schematic diagram of modifying the surface of $Li_{1.2}Ni_{0.2}Mn_{0.6}O_2$ by spinel $Li_4Mn_5O_{12}$.

2. Experimental

2.1. Preparation of the $Li_{1.2}Mn_{0.6}Ni_{0.2}O_2$

Weigh 0.24 mol of lithium acetate dihydrate, 0.04 mol of nickel acetate tetrahydrate, and 0.12 mol of manganese acetate tetrahydrate according to the chemical formula $Li_{1.2}Mn_{0.6}Ni_{0.2}O_2$, and use magnetic stirring to completely dissolve them in 180 mL of deionized water. Then, 0.4 mol of complexing agent citric acid monohydrate is weighed and completely dissolved in 20 mL of deionized water by stirring. Next, slowly pour the citric acid solution into the salt mixture and stir until the mixture is smooth. Add an appropriate amount of nitric acid solution, stir, and react in a water bath at 80 °C to obtain a yellow-green transparent gel. Then, dry it in a blast oven at 160 °C for 12 h to obtain a dry gel precursor. Finally, after the precursor is fully ground, it is put into a muffle furnace under an air atmosphere and preheated at 3 °C·min^{-1} to 500 °C for 5 h to obtain the metal oxide precursor. Finally, the precursor is calcined at 900 °C for 12 h at the same heating rate to obtain the $Li_{1.2}Mn_{0.6}Ni_{0.2}O_2$ material.

2.2. Preparation of $Li_4Mn_5O_{12}/Li_{1.2}Mn_{0.6}Ni_{0.2}O_2$ Materials

According to the chemical formula $0.03Li_4Mn_5O_{12}\cdot0.97Li_{1.2}Ni_{0.2}Mn_{0.6}O_2$, weigh 1.0 g of active material, 0.15 g of lithium acetate dihydrate, 0.45 g of manganese acetate tetrahydrate, 0.20 g of polyvinylpyrrolidone, and 20 g of ethanol and mix them evenly with a magnetic stirrer to obtain a mixed solution. Then, in order to obtain the precursor, the mixed solution is heated in a water bath at 80 °C until the solvent ethanol is completely volatilized. Finally, the obtained precursor is calcined at 5 °C·min^{-1} to 450 °C for 5 h under an air atmosphere to obtain the spinel $Li_4Mn_5O_{12}/Li_{1.2}Mn_{0.6}Ni_{0.2}O_2$ material. By adjusting the ratio of $Li_4Mn_5O_{12}$ and $Li_{1.2}Ni_{0.2}Mn_{0.6}O_2$, the content of the surface modification layer of the active material is controlled. According to the ratio of $Li_4Mn_5O_{12}$ and $Li_{1.2}Ni_{0.2}Mn_{0.6}O_2$, the three components are 0.01:0.99, 0.03:0.97, and 0.05:0.95 which are

recorded as LMO@LNM-1%, LMO@LNM-3%, and LMO@LNM-5%, respectively, while the unmodified sample is recorded as LNM.

2.3. Preparation and Assembly of Electrodes

The working electrode is composed of sample (80 wt.%), carbon black (super-P, 10 wt.%), and polyvinylidene fluoride (PVDF, 10 wt.%) mixed in N-methyl pyrrolidone (NMP) to prepare a slurry. Then, evenly coat the slurry on aluminum foil with a thickness of approximately 150 μm, and then vacuum dry it at 80 °C for 12 h. With lithium metal sheet as the counter electrode, 1M lithium hexafluorophosphate ($LiPF_6$) is dissolved in a mixture of ethylene carbonate (EC), methyl ethyl carbonate (EMC), and dimethyl carbonate (DMC) with a volume ratio of 1:1:1 as the electrolyte. The Celgard 2400 serves as a diaphragm. The battery is assembled in a glove box filled with argon gas.

2.4. Characterization and Testing of Materials

The crystal structure of the samples was analyzed by powder X-ray diffractometer (XRD, Model X′pert 3, Cu-Kα radiation: $2° \cdot min^{-1}$, 10–90°). The morphology of the samples was characterized by field emission scanning electron microscopy (SEM, Hitachi SU8100 USA EDAX). The composition, distribution, and relative content of the elements on the sample surface can be obtained by using the X-ray energy spectrometer (EDS) equipped with the scanning electron microscope. The surface composition and elemental valence were measured using X-ray photoelectron spectroscopy (XPS). The crystal plane spacing and the phase of the sample were determined using transmission electron microscopy (TEM, JEOL 1011).

CR-2032 half-cell was used to test electrochemical performance. The charge and discharge test was carried out using the Blue Electric Battery Test System (CT2001A LAND). Cyclic voltammetry (CV) was tested using the Shanghai Chenhua Electrochemistry workstation with an electrochemical window of 2.0–4.8 V and a scanning rate of $0.1 \text{ mV} \cdot s^{-1}$. Electrochemical impedance spectroscopy (EIS, 0.01–100k Hz) was measured with a CHI660E Electrochemical workstation (Shanghai, China, Chenhua).
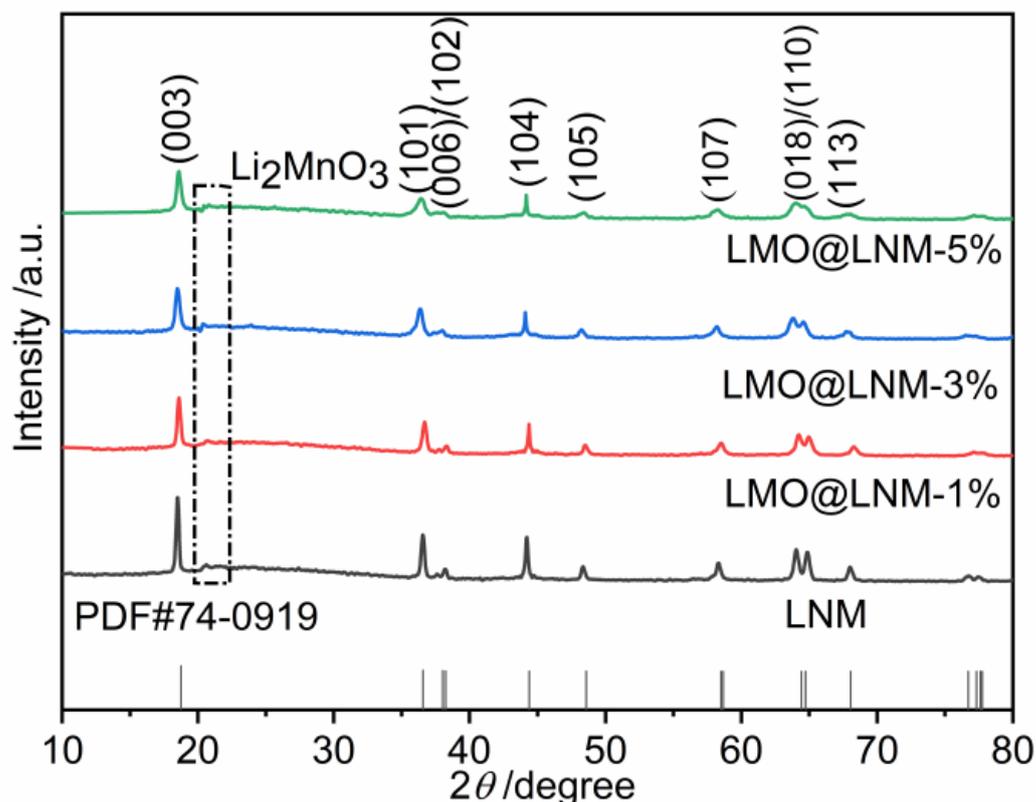
3. Results and Discussion

3.1. X-ray Diffraction Analysis

The crystal phases of the pristine and the modified samples are shown in Figure 2. Compared with the standard PDF#74-0919 and the LNM, the LMO@LNM-1%, LMO@LNM-3%, and LMO@LNM-5% samples exhibit the characteristic peaks of the $LiMO_2$ (M=Ni, Mn) phase of the typical layered hexagonal α-$NaFeO_2$ structures with space groups R-3m [26]. We can observe the weak lithium-rich diffraction peak with the diffraction angle of 20–25° [34]. At the same time, the (006)/(102) and (018)/(110) diffraction peaks appear in pairs in the XRD images, indicating that the prepared materials have ordered layered structures [35]. However, the intensities of the corresponding (003) and (104) diffraction peaks decrease as the relative content of spinel $Li_4Mn_5O_{12}$ increases. There is no spinel $Li_4Mn_5O_{12}$ phase in the XRD patterns of the LMO@LNM-1%, LMO@LNM-3%, and LMO@LNM-5% samples, possibly because the content of the surface modification layer is low and it is not easy to detect. In general, no impurity peaks are found in the XRD patterns of the three samples, indicating that the modified layer would not induce the formation of new phases in the samples.

The lattice parameter (*a*, *c*, *c/a*) values and the $I_{(003)}/I_{(104)}$ values of the three samples with different component ratios, along with those of the unmodified samples, can be obtained by fitting and calculating the XRD test results using Jade, as shown in Table S1 (Supplementary Materials). It is obvious that the lattice parameter *c/a* values of the four samples are greater than 4.899, which also indicates that the obtained sample materials have well-ordered layered structures [36,37]. Meanwhile, the $I_{(003)}/I_{(104)}$ values of the four samples are all greater than 1.2, indicating that the samples have high cation ordering. In addition, as the proportion of the component increases, the $I_{(003)}/I_{(104)}$ value of the samples

gradually increases. In summary, the four samples have a good lamellar structure and high cation ordering. Moreover, as the component content ratio increases, the $I_{(003)}/I_{(104)}$ value of the sample gradually increases, indicating that the higher component ratio may help reduce the degree of cation mixing in the material. The moderate component ratio may be conducive to the formation of materials with good crystal structure and cationic ordering.
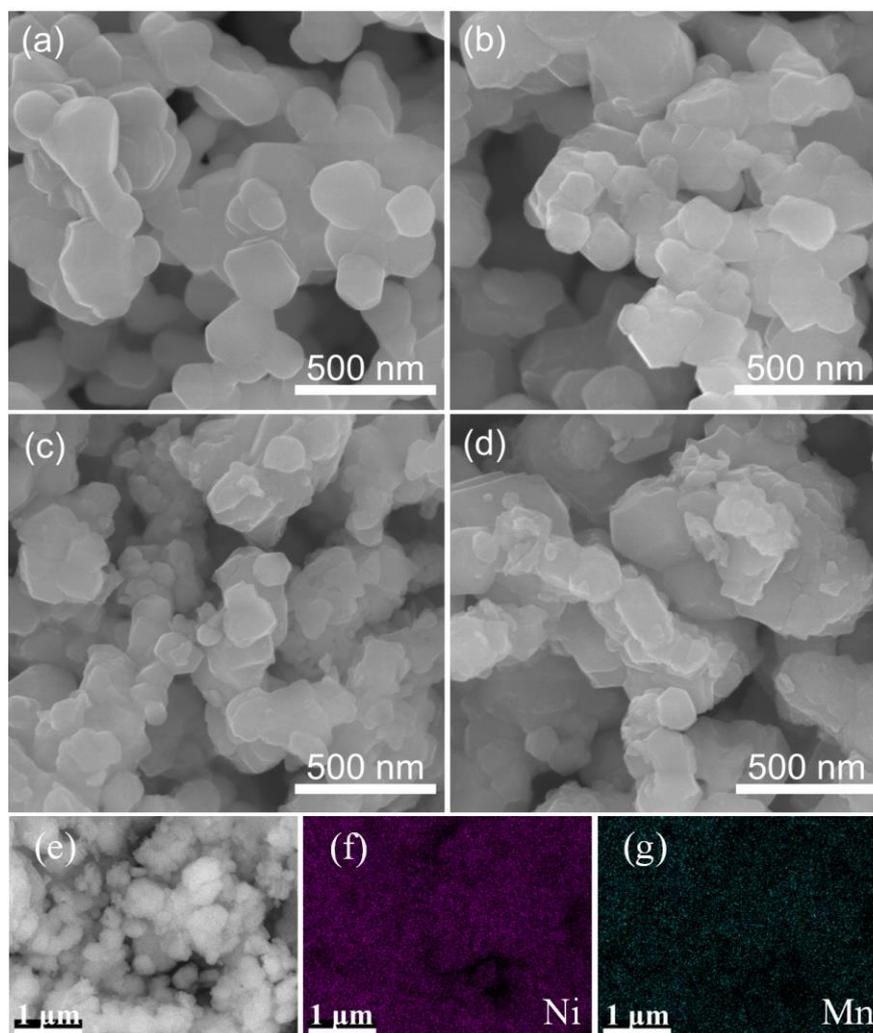

Figure 2. X-ray diffraction patterns of LNM, LMO@LNM-1%, LMO@LNM-3%, and LMO@LNM-5%.

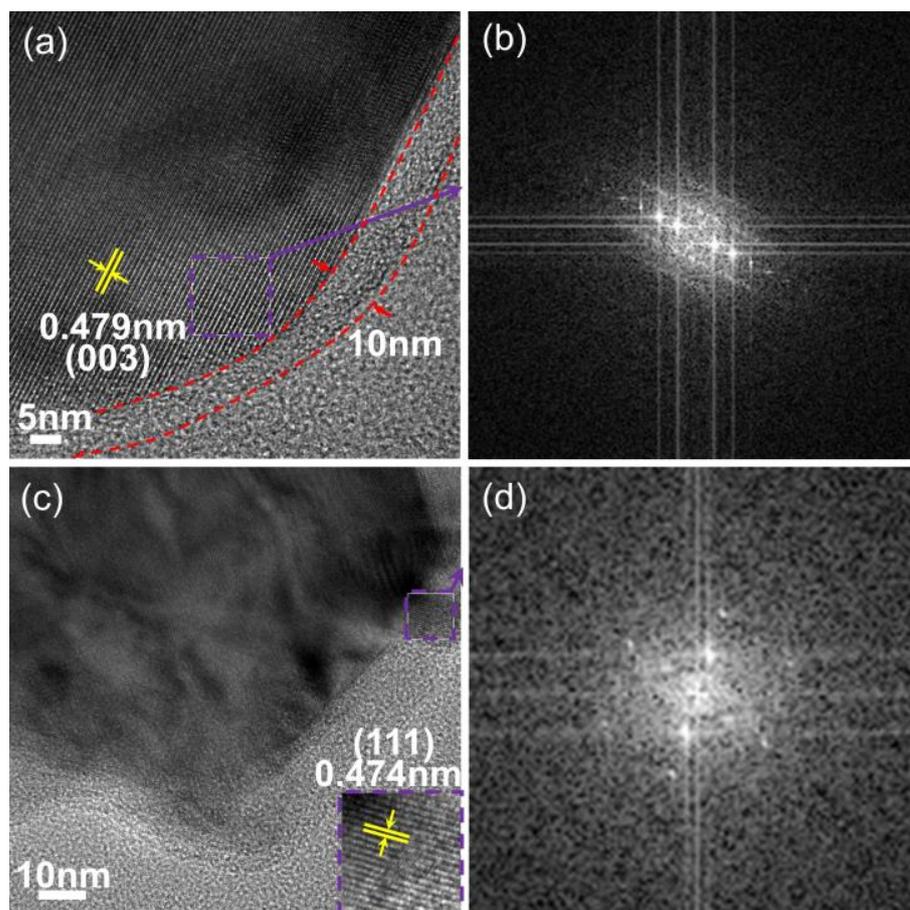### 3.2. Material Morphology and Composition Analysis

Figure 3 shows SEM images of the LNM, LMO@LNM-1%, LMO@LNM-3%, and LMO@LNM-5% samples. It can be seen that, compared with the LNM samples, there are no significant differences in the morphologies of the LMO@LNM-1%, LMO@LNM-3%, and LMO@LNM-5% samples. The surface of the primary particles is polygonal, while the secondary particles are stacked by the primary particles, showing a prism-like structure. However, with the increase in the $Li_4Mn_5O_{12}$ component proportion, the agglomeration degree of the secondary particles increased, and the roughness and compactness of the material surface increased, as shown in Figure S1. At the same time, these will lead to a decrease in crystallinity, which would be detrimental to the diffusion of Li ions in the material.

Mapping scan was performed for the LMO@LNM-3% samples, as shown in Figure 3e–g. It can be seen that the Mn and Ni elements are uniformly distributed on the surface of the LMO@LNM-3% samples, indicating the homogeneity of the spinel $Li_4Mn_5O_{12}$ surface modification process. The test results show that the contents of Mn and Ni are 79.84% and 20.16%, respectively, which correspond to the stoichiometric ratio of the LMO@LNM-3% samples.

Figure 3. SEM images of samples (**a**) LNM, (**b**) LMO@LNM-1%, (**c**) LMO@LNM-3%, (**d**) LMO@LNM-5%. EDS image of LMO@LNM-3% sample (**e**–**g**).
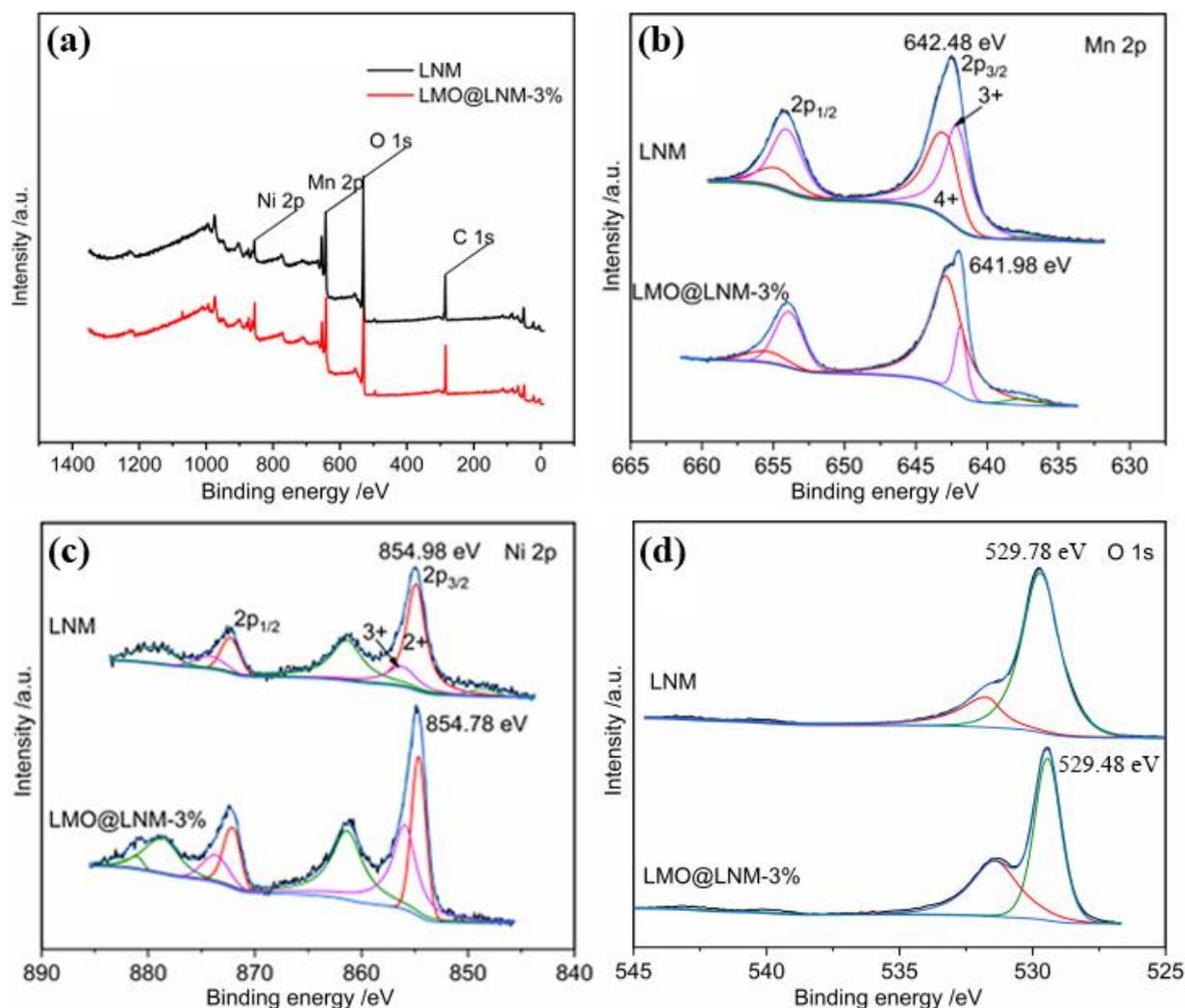
The surface morphology and crystal structure of the LMO@LNM-3% primary particles are further studied by TEM. Figure 4a,c are high-resolution TEM (HRTEM) images of the LMO@LNM-3% samples. It can be seen from Figure 4a that a light-gray thin layer is uniformly formed on the surface of the LMO@LNM-3% sample, which is obviously different from the bulk particles. The thickness is approximately 10 nm, which proves the existence of the coating layer. In addition, it can be seen that the primary particles of the LMO@LNM-3% sample show a clear lattice fringe, showing an obvious lamellar structure. Fast Fourier Transform (FFT) was applied to the purple frame region of the particle body, and the analysis results are shown in Figure 4b. The interplanar distance of the lattice fringe of the LMO@LNM-3% sample is 0.479 nm, corresponding to the crystal plane (003) in the layered oxide structure. Then, as shown in Figure 4c, by magnifying the edge of the light-gray composite modification interface, it is observed that there are some lattice fringes in the composite modification interface layer. Next, FFT was performed on the purple frame selection area of the composite thin layer. As shown in Figure 4d, the crystal plane spacing is 0.474 nm, corresponding to the (111) crystal plane of the $Li_4Mn_5O_{12}$ crystal [38]. Therefore, spinel $Li_4Mn_5O_{12}$ exists in the coating layer. However, the spinel $Li_4Mn_5O_{12}$ crystal is unevenly distributed on the surface of the raw material particles, which may be caused by the uneven dispersion of the raw material particles in the mixed solution.

Figure 4. TEM images of LMO@LNM-3% (**a**,**c**) and FFT images of LMO@LNM-3% (**b**,**d**).

XPS was used to study the surface composition and elemental valence of the LNM and LMO@LNM-3% samples [39], and Avantage fitting results are shown in Figure 5. Figure 5a shows the XPS survey scans of the LNM and LMO@LNM-3% samples, which also proves the presence of the Ni, Mn, and O elements, while the high intensity O 1s peak indicates that both samples are stable oxides. Figure 5b shows the fine spectra of Mn 2p of the two samples. The binding energies of their characteristic peaks are 642.48 eV and 641.98 eV which are consistent with the characteristic binding energies of Mn 2p [40]. Compared with the Mn 2p binding energy of the LNM samples, the Mn 2p characteristic peak of the LMO@LNM-3% samples shifted to the right, indicating that the binding energy of the LMO@LNM-3% samples decreased. In addition, it can be seen from the fitting results that Mn^{3+} and Mn^{4+} exist in both the LNM and the LMO@LNM-3% samples. Compared with the relative contents of the two valence states of Mn in the LNM samples, the content of Mn^{4+} in the LMO@LNM-3% samples is significantly higher than that of Mn^{3+}. This shows that the crystal structure stability of the LMO@LNM-3% sample has been improved, which is consistent with the XRD analysis results. Figure 5c shows the fine spectrum of Ni 2p in the samples. The characteristic peaks observed at binding energies of 854.98 eV and 854.78 eV correspond to the characteristic binding energies of Ni 2p. Compared with the Ni 2p binding energy of the LNM sample, the Ni 2p characteristic peak of the LMO@LNM-3% sample also shifted to the right, which also indicates that the binding energy of the LMO@LNM-3% sample decreased. At the same time, it can be seen from the fitting results that Ni^{2+} and Ni^{3+} exist in the LNM and LMO@LNM-3% samples. Compared with the relative contents of the two valence states of Ni in the LNM sample, the relative content of Ni^{2+} in the LMO@LNM-3% sample is significantly reduced, which is helpful to improve the cationic ordering of the materials, which is consistent with the XRD analysis results.

Figure 5d shows the fine O 1s spectra of the LNM and LMO@LNM-3% samples. It can be seen that the characteristic peak binding-energies of O 1s of the two samples are 529.78 eV and 529.48 eV. The O 1s characteristic peak of the LNMO-3% samples shifted to the right and the binding energy decreased. Since the characteristic peaks of O 1s of the two samples are not significantly different, this indicates that the surface components are all metal oxides, which is consistent with the TEM test results of the LMO@LNM-3% sample.
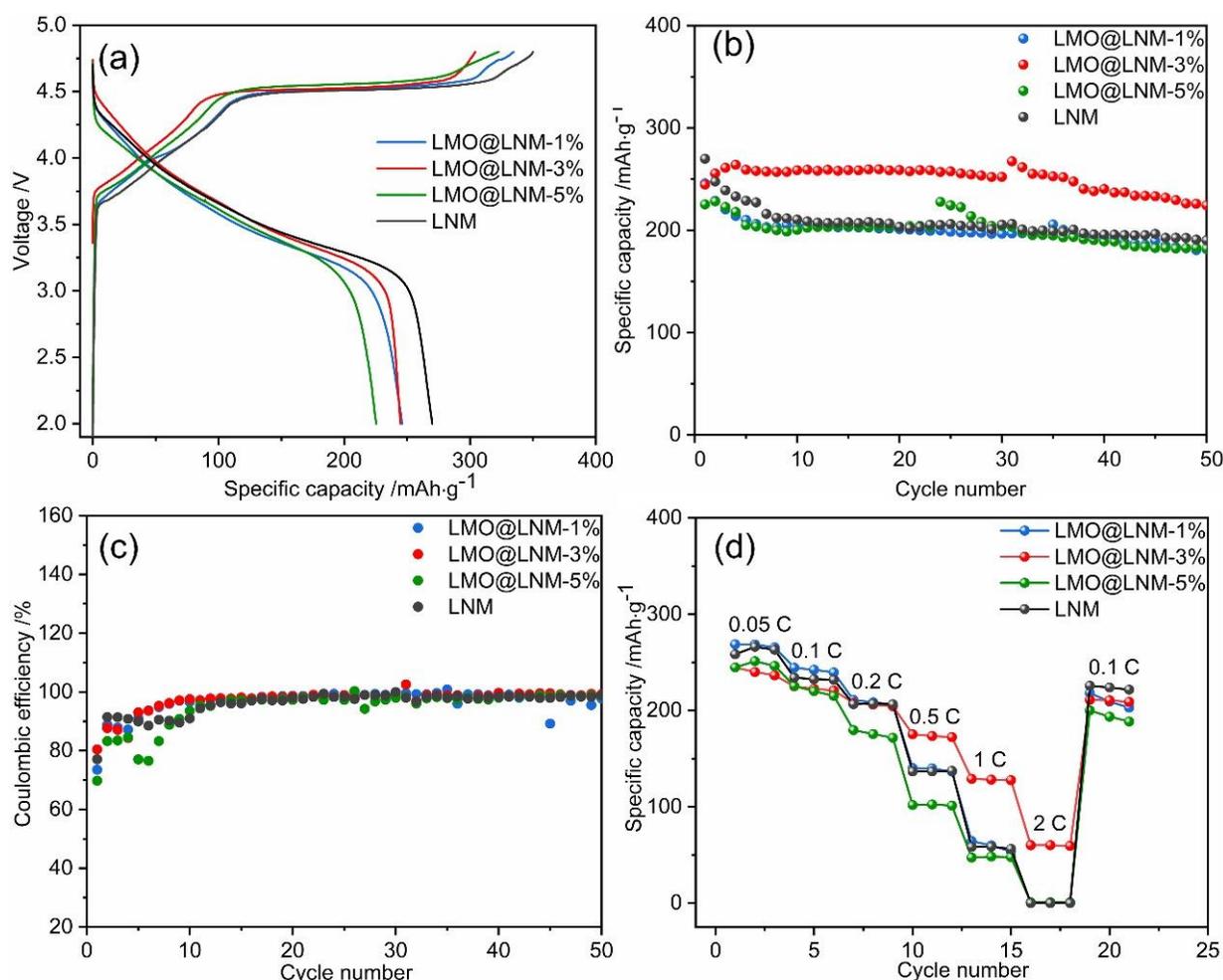

Figure 5. XPS spectra of LNM and LMO@LNM-3% (**a**) Full spectrum, (**b**) Mn 2p spectrum, (**c**) Ni 2p spectrum, (**d**) O 1s spectrum.

3.3. Electrochemical Characterization

The electrochemical cycle test is used to study the effect of spinel $Li_4Mn_5O_{12}$ coating on the electrochemical properties of raw materials. Figure 6a shows the first charging and discharging curves of the LNM, LMO@LNM-1%, LMO@LNM-3%, and LMO@LNM-5% samples at the current density of 12.5 mA·g^{-1}. During the first charging process, the diagonal below 4.5 V and the high potential platform at 4.5 V are associated with the reversible extraction of Li ions from the layered structure of lithium. The diagonal line higher than 4.5 V corresponds to the irreversible activation and oxygen loss of Li_2MnO_3 [41,42]. In addition, the first discharge capacity of the LNM, LMO@LNM-1%, LMO@LNM-3%, and LMO@LNM-5% samples are 269.9 mAh·g^{-1}, 246.0 mAh·g^{-1}, 244.7 mAh·g^{-1}, and 225.3 mAh·g^{-1}, respectively. Compared with the first discharge capacity of the LNM samples, the first discharge capacity of the LMO@LNM-1%, LMO@LNM-3%, and LMO@LNM-5% samples are decreased to some

extent, which may be due to the decrease in active material content, caused by the increase in spinel $Li_4Mn_5O_{12}$.

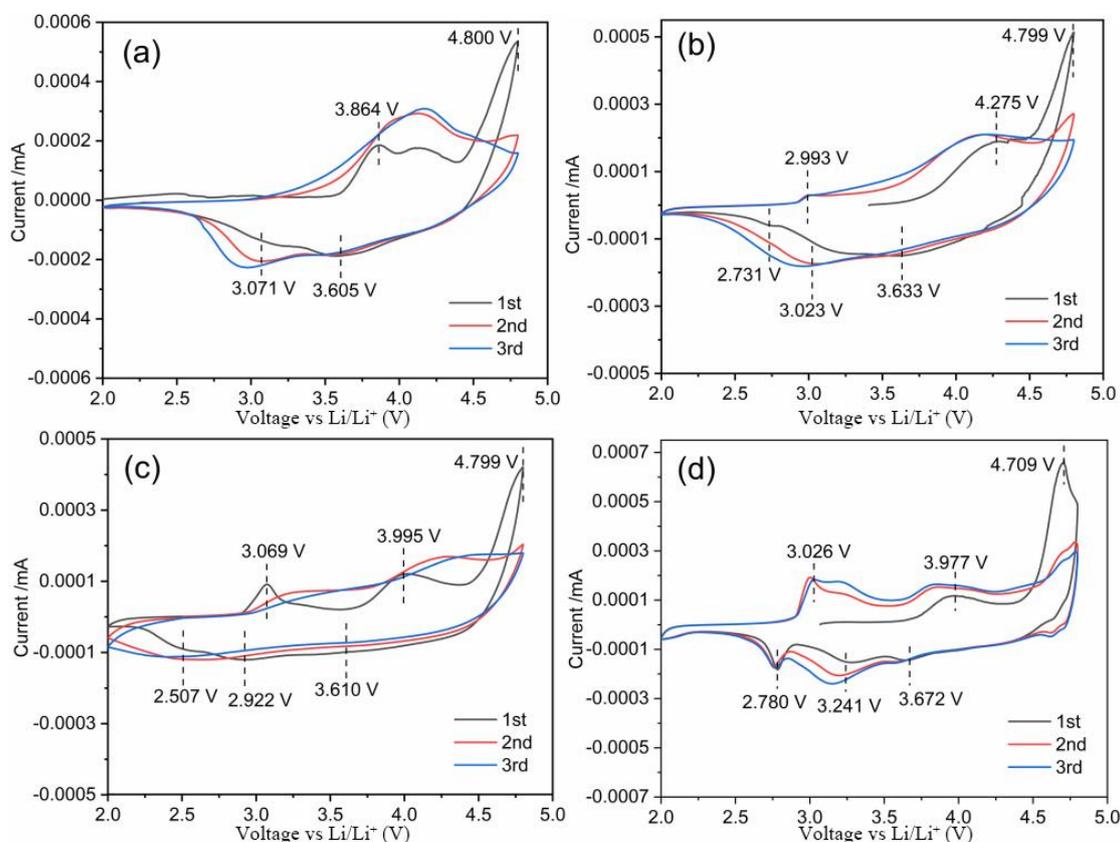**Figure 6.** Cycle performance curves of the samples (**a**) initial charge−discharge curve at 0.05 C, (**b**) discharge specific capacity, (**c**) coulombic efficiency curve at 0.05 C, (**d**) cycling capacity.

It can be seen from Figure 6b that after 50 charge and discharge cycles, the capacity retention rates of the LNM, LMO@LNM-1%, LMO@LNM-3%, and LMO@LNM-5% samples are 70.51%, 73.82%, 91.74%, and 80.87%, respectively. Compared with the LNM samples, the LMO@LNM-3% samples show a significant improvement in cyclic performance. This may be due to the large c/a and $I_{(003)}/I_{(104)}$ values of the LMO@LNM-3% samples, indicating that the sample has a highly ordered layered structure and a high cation ordering, thus showing good cycling stability. As shown in Figure 6c, the first coulomb efficiencies of the LNM, LMO@LNM-1%, LMO@LNM-3%, and LMO@LNM-5% samples are 77.1%, 73.53%, 80.46%, and 69.8%, respectively. The high relative content of Mn^{4+} in its crystal structure, which increases the stability of the material's crystal structure and reduces oxygen loss, thus leading to the first coulomb efficiency of the LMO@LNM-3% samples, is the highest. Therefore, it has effectively improved the first coulomb efficiency of the LMO@LNM-3% samples. In general, the LMO@LNM-3% samples have the highest first coulomb efficiency and capacity retention rates, indicating that spinel $Li_4Mn_5O_{12}$ modified layer is helpful in improving the lamellar structure stability and cation ordering of raw materials, thus improving the cyclic stability of materials.

The rate performances of the four samples are shown in Figure 6d. It can be seen that at low current densities of 0.05 C, 0.1 C and 0.2 C, the specific discharge capacity of the LMO@LNM-1%, LMO@LNM-3%, and LMO@LNM-5% samples decreases with the increase

in spinel $Li_4Mn_5O_{12}$ modified layer content. This can be attributed to the fact that the modified layer formed on the surface of the raw material particles has a greater resistance to the diffusion of lithium ions in the material at a lower current density. At large current densities of 0.5 C, 1 C, and 2 C, compared with the LNM samples, the LMO@LNM-3% samples show a higher specific discharge capacity, indicating that the surface modification layer is beneficial for Li ion diffusion in the material at large current densities.
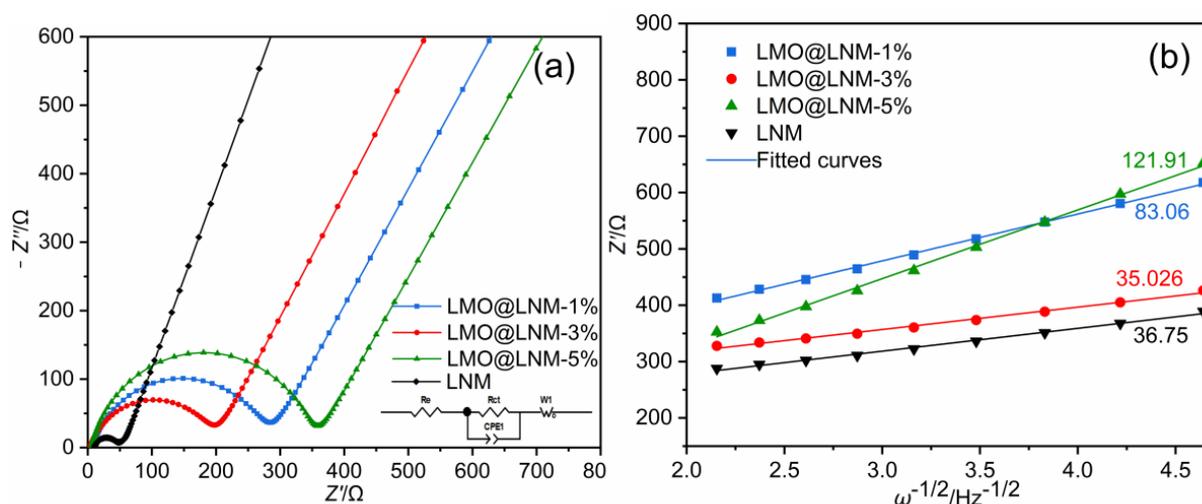
We further explored the redox process of the LNM, LMO@LNM-1%, LMO@LNM-3%, and LMO@LNM-5% samples, and conducted a cyclic voltammetry (CV) test on four samples. As shown in Figure 7, within the voltage range of 2.0−4.8 V, two obvious anode peaks appeared at 3.8−4.3 V and 4.5−4.8 V during the first charging of the four samples. The first anodic peak of approximately 4.0 V corresponds to the Ni^{3+}/Ni^{4+} oxidation reaction, accompanied by the extraction of lithium ions from the layered metal oxide structure, and corresponds to the first voltage plateau at the first charge [43]. The second anodic peak of approximately 4.8 V corresponds to the irreversible activation of Li_2MnO_3 and the loss of oxygen [44]. Moreover, the two cathodic peaks of approximately 3.6 V and 3.0 V correspond to the reduction reaction of Ni^{4+}/Ni^{3+} and Mn^{4+}/Mn^{3+}, respectively. In addition, compared with the LNM samples, a new anodic peak is generated at a voltage of approximately 3.0 V during the charge-discharge cycles for the LMO@LNM-1%, LMO@LNM-3%, and LMO@LNM-5% samples. These results indicate that new oxidation reactions corresponding to different electric potentials occur during the charging process, and similar phenomena occur during the discharge process, which may be related to the spinel $Li_4Mn_5O_{12}$ modified layer. The redox peaks of the LMO@LNMO-3% samples are obvious, and the area of the closed curve increases obviously with the increase in the number of cycles. This indicates that the electrode material is gradually activated and the discharge specific capacity increases, which is consistent with the cycle performance of the material.

Figure 7. CV curves of samples (**a**) LNM, (**b**) LMO@LNM−1%, (**c**) LMO@LNM−3%, (**d**) LMO@LNM−5%.

To further investigate the electrode reaction kinetics of the LNM, LMO@LNM-1%, LMO@LNM-3%, and LMO@LNM-5% samples, electrochemical impedance tests were performed. Figure 8a shows the EIS curves of the four samples. It can be found that the EIS curves of the materials are represented by semicircles at high-medium frequencies and by inclined lines at low frequencies. The intersection point between the starting point of the high-medium frequencies and the real axis is R_e, the semicircle corresponds to R_{ct}, and the inclined lines at low-frequencies represent Z_w [26]. In addition, the impedance parameters, Weber coefficient (Figure 8b), and the Li ion diffusion coefficient of the samples can be obtained by fitting and by Equation (1) [45,46]:

$$D_{Li^+} = \frac{R^2 T^2}{2A^2 n^4 F^4 C^2 \sigma^2} \tag{1}$$

Figure 8. Electrochemical impedance performance of the samples (**a**) EIS spectrum, (**b**) Weber coefficient relationship curve.

$D_{Li}{}^+$, R, T, A, n, F, C and σ represent the Li ion diffusion coefficient, gas constant, room temperature, electrode surface area, number of electrons transferred in the reaction, Faraday constant, lithium ion concentration, and Weber coefficient, respectively [47,48].

The fitted impedance parameters, Weber coefficient, and the lithium ion diffusion coefficient of the four samples are shown in Table S2. It can be seen that the difference of R_e among the four samples is not significant. The R_{ct} values of the four samples are 31.46 Ω, 273.0 Ω, 192.6 Ω, and 346.6 Ω, respectively. Compared with LNM samples, the charge transfer impedances of the LMO@LNM-1%, LMO@LNM-3%, and LMO@LNM-5% samples are significantly increased. R_{ct} represents the impedance of Li$^+$ passing through the SEI film on the surface of the active material [49]. The increase in R_{ct} indicates that the interface charge transfer is blocked, which may be related to the modification layer of spinel Li$_4$Mn$_5$O$_{12}$. Meanwhile, the $D_{Li}{}^+$ of the four samples are 8.32×10^{-15} cm^2·s^{-1}, 1.63×10^{-15} cm^2·s^{-1}, 9.16×10^{-15} cm^2·s^{-1}, and 6.98×10^{-15} cm^2·s^{-1}, respectively. Obviously, the LMO@LNM-3% samples have a larger $D_{Li}{}^+$. This shows that it has a fast diffusion rate of Li$^+$ and good electrochemical performance, which is consistent with the results of the sample rate performance test.

4. Conclusions

In summary, this study successfully prepared spinel Li$_4$Mn$_5$O$_{12}$ surface-modified Li$_{1.2}$Ni$_{0.2}$Mn$_{0.6}$O$_2$ material by the wet chemical method. The results show that the ultrathin spinel Li$_4$Mn$_5$O$_{12}$ shell can reduce oxygen loss during the first cycle and improve the cation ordering of the material. Therefore, the first coulomb efficiency of Li$_4$Mn$_5$O$_{12}$/Li$_{1.2}$Ni$_{0.2}$Mn$_{0.6}$O$_2$ material at the current density of 12.5 mA·g^{-1} is 80.46%,

and the capacity retention rate after 50 cycles can reach 91.74%. Compared with the raw material, it has increased by 3.36% and 21.23% showing better electrochemical reversibility and cycle stability. At the same time, the LMO@LNM-3% samples show high discharge specific capacity at high current density, which indicates that the spinel $Li_4Mn_5O_{12}$ surface modification layer contributes to the improvement of material rate properties. Therefore, this study provides a simple modification method for improving the stability of cobalt-free lithium-rich manganese cathode material, which has a good application prospect.

Supplementary Materials: The following supporting information can be downloaded at: https://www.mdpi.com/xxx/s1. Figure S1: Low magnification SEM images of (a) LNM, (b) LMO@LNM-1%, (c) LMO@LNM-3%, (d) LMO@LNM-5%; Table S1: Lattice parameters and characteristic peak ratios of the LNM; Table S2: Fitted impedance parameters, weber coefficients, and lithium-ion diffusion coefficients for the samples.

Author Contributions: Conceptualization, Y.Q., X.P., L.Z. and L.B.; methodology, Y.Q., L.Z. and J.Y.; data curation, Y.Q., X.P. and Y.S.; formal analysis, Y.Q., X.P. and X.L.; investigation, J.Y., L.H., Q.X. and L.B.; writing—original draft, Y.Q.; writing—review and editing, L.Z., Y.S., S.W. and J.L.; funding acquisition, S.W. and J.L. All authors have read and agreed to the published version of the manuscript.

Data Availability Statement: Not applicable.

Conflicts of Interest: The authors declare that they have no known competing financial interests or personal relationships that could have appeared to influence the work reported in this paper.

References

1. Wang, S.; Wang, Y.; Song, Y.; Jia, X.; Yang, J.; Li, Y.; Liao, J.; Song, H. Immobilizing Polysulfide via Multiple Active Sites in W18O49 for Li-S batteries by Oxygen Vacancy Engineering. *Energy Storage Mater.* **2021**, *43*, 422–429. [CrossRef]
2. Huang, B.; Pan, Z.; Su, X.; An, L. Recycling of lithium-ion batteries: Recent advances and perspectives. *J. Power Sources* **2018**, *399*, 274–286. [CrossRef]
3. Wu, F.; Li, Q.; Chen, L.; Zhang, Q.; Wang, Z.; Lu, Y.; Bao, L.; Chen, S.; Su, Y. Improving the Structure Stability of $LiNi_{0.8}Co_{0.1}Mn_{0.1}O_2$ by Surface Perovskite-like $La_2Ni_{0.5}Li_{0.5}O_4$ Self-Assembling and Subsurface La^{3+} Doping. *ACS Appl. Mater. Interfaces* **2019**, *11*, 36751–36762. [CrossRef] [PubMed]
4. Li, L.; Tan, H.; Yuan, X.; Ma, H.; Ma, Z.; Zhao, Y.; Zhao, J.; Wang, X.; Chen, D.; Dong, Y. Direct ink writing preparation of LiFePO4/MWCNTs electrodes with high-areal Li-ion capacity. *Ceram. Int.* **2021**, *47*, 21161–21166. [CrossRef]
5. Wang, S.; Feng, S.; Liang, J.; Su, Q.; Zhao, F.; Song, H.; Zheng, M.; Sun, Q.; Song, Z.; Jia, X.; et al. Insight into MoS_2–MoN Heterostructure to Accelerate Polysulfide Conversion toward High-Energy-Density Lithium–Sulfur Batteries. *Adv. Energy Mater.* **2021**, *11*, 2003314. [CrossRef]
6. Yao, Y.; Wang, S.; Jia, X.; Yang, J.; Li, Y.; Liao, J.; Song, H. Freestanding sandwich-like hierarchically TiS2–TiO2/Mxene bi-functional interlayer for stable Li–S batteries. *Carbon* **2022**, *188*, 533–542. [CrossRef]
7. Chen, R.; Zhao, T.; Zhang, X.; Li, L.; Wu, F. Advanced cathode materials for lithium-ion batteries using nanoarchitectonics. *Nanoscale Horiz.* **2016**, *1*, 423–444. [CrossRef]
8. Goodenough, J.B.; Kim, Y. Challenges for Rechargeable Li Batteries. *Chem. Mater.* **2009**, *22*, 587–603. [CrossRef]
9. Wang, S.; Liao, J.; Yang, X.; Liang, J.; Sun, Q.; Liang, J.; Zhao, F.; Koo, A.; Kong, F.; Yao, Y.; et al. Designing a highly efficient polysulfide conversion catalyst with paramontroseite for high-performance and long-life lithium-sulfur batteries. *Nano Energy* **2018**, *57*, 230–240. [CrossRef]
10. Bi, L.; Wei, X.; Qiu, Y.; Song, Y.; Long, X.; Chen, Z.; Wang, S.; Liao, J. A highly ionic transference number eutectogel hybrid electrolytes based on spontaneous coupling inhibitor for solid-state lithium metal batteries. *Nano Res.* **2022**, *16*, 1717–1725. [CrossRef]
11. Padhi, A.K.; Nanjundaswamy, K.S.; Goodenough, J.B. Phospho-olivines as Positive-Electrode Materials for Rechargeable Lithium Batteries. *J. Electrochem. Soc.* **1997**, *144*, 1188–1194. [CrossRef]

12. Antolini, E. LiCoO$_2$: Formation, structure, lithium and oxygen nonstoichiometry, electrochemical behaviour and transport properties. *Solid State Ionics* **2004**, *170*, 159–171. [CrossRef]

13. Amatucci, G.G.; Tarascon, J.-M. Optimization of Insertion Compounds Such as LiMn[sub 2]O[sub 4] for Li-Ion Batteries. *J. Electrochem. Soc.* **2002**, *149*, K31–K46. [CrossRef]

14. Karunawan, J.; Abdillah, O.B.; Floweri, O.; Aji, M.P.; Santosa, S.P.; Sumboja, A.; Iskandar, F. Improving the Structural Ordering and Particle-Size Homogeneity of Li-Rich Layered Li$_{1.2}$Ni$_{0.13}$Co$_{0.13}$Mn$_{0.54}$O$_2$ Cathode Materials through Microwave Irradiation Solid-State Synthesis. *Batteries* **2022**, *9*, 31. [CrossRef]

15. Yu, H.; Zhou, H. High-Energy Cathode Materials (Li$_2$MnO$_3$–LiMO$_2$) for Lithium-Ion Batteries. *J. Phys. Chem. Lett.* **2013**, *4*, 1268–1280. [CrossRef]

16. Wang, S.; Wang, Y.; Song, Y.; Zhang, J.; Jia, X.; Yang, J.; Shao, D.; Li, Y.; Liao, J.; Song, H. Synergistic regulating of dynamic trajectory and lithiophilic nucleation by Heusler alloy for dendrite-free Li deposition. *Energy Storage Mater.* **2022**, *50*, 505–513. [CrossRef]

17. Wang, S.; Chen, H.; Liao, J.; Sun, Q.; Zhao, F.; Luo, J.; Lin, X.; Niu, X.; Wu, M.; Li, R.; et al. Efficient Trapping and Catalytic Conversion of Polysulfides by VS$_4$ Nanosites for Li–S Batteries. *ACS Energy Lett.* **2019**, *4*, 755–762. [CrossRef]

18. Ates, M.N.; Mukerjee, S.; Abraham, K.M. A Search for the Optimum Lithium Rich Layered Metal Oxide Cathode Material for Li-Ion Batteries. *J. Electrochem. Soc.* **2015**, *162*, A1236–A1245. [CrossRef]

19. Boulineau, A.; Simonin, L.; Colin, J.-F.; Bourbon, C.; Patoux, S. First Evidence of Manganese–Nickel Segregation and Densification upon Cycling in Li-Rich Layered Oxides for Lithium Batteries. *Nano Lett.* **2013**, *13*, 3857–3863. [CrossRef]

20. Zhang, K.; Han, X.; Hu, Z.; Zhang, X.; Tao, Z.; Chen, J. Nanostructured Mn-based oxides for electrochemical energy storage and conversion. *Chem. Soc. Rev.* **2014**, *44*, 699–728. [CrossRef]

21. Li, X.; Qiao, Y.; Guo, S.; Xu, Z.; Zhu, H.; Zhang, X.; Yuan, Y.; He, P.; Ishida, M.; Zhou, H. Direct Visualization of the Reversible O^{2-}/O$^-$ Redox Process in Li-Rich Cathode Materials. *Adv. Mater.* **2018**, *30*, e1705197. [CrossRef] [PubMed]

22. Lu, Z.; MacNeil, D.D.; Dahn, J.R. Layered Li[Ni[sub x]Co[sub 1−2x]Mn[sub x]]O[sub 2] Cathode Materials for Lithium-Ion Batteries. *Electrochem. Solid-state Lett.* **2001**, *4*, A200–A203. [CrossRef]

23. Ji, X.; Xia, Q.; Xu, Y.; Feng, H.; Wang, P.; Tan, Q. A review on progress of lithium-rich manganese-based cathodes for lithium ion batteries. *J. Power Sources* **2020**, *487*, 229362. [CrossRef]

24. He, W.; Yuan, D.; Qian, J.; Ai, X.; Yang, H.; Cao, Y. Enhanced high-rate capability and cycling stability of Na-stabilized layered Li1.2[Co0.13Ni0.13Mn0.54]O2 cathode material. *J. Mater. Chem. A* **2013**, *1*, 11397–11403. [CrossRef]

25. Zhu, W.; Tai, Z.; Shu, C.; Chong, S.; Guo, S.; Ji, L.; Chen, Y.; Liu, Y. The superior electrochemical performance of a Li-rich layered cathode material with Li-rich spinel Li$_4$Mn$_5$O$_{12}$ and MgF$_2$ double surface modifications. *J. Mater. Chem. A* **2020**, *8*, 7991–8001. [CrossRef]

26. Ding, G.; Yan, F.; Zhu, Z.; Chen, J.; Hu, Z.; Li, G.; Liu, J.; Gao, L.; Jiang, W.; Sun, F. Mussel-inspired polydopamine-assisted uniform coating of Li+ conductive LiAlO2 on nickel-rich LiNi0.8Co0.1Mn0.1O2 for high-performance Li-ion batteries. *Ceram. Int.* **2021**, *48*, 5714–5723. [CrossRef]

27. Akkinepally, B.; Reddy, I.N.; Ko, T.J.; Yoo, K.; Shim, J. Dopant effect on Li+ ion transport in NASICON-type solid electrolyte: Insights from molecular dynamics simulations and experiments. *Ceram. Int.* **2022**, *48*, 12142–12151. [CrossRef]

28. Li, Q.; Li, G.; Fu, C.; Luo, D.; Fan, J.; Li, L. K$^+$-Doped Li$_{1.2}$Mn$_{0.54}$Co$_{0.13}$Ni$_{0.13}$O$_2$: A Novel Cathode Material with an Enhanced Cycling Stability for Lithium-Ion Batteries. *ACS Appl. Mater. Interfaces* **2014**, *6*, 10330–10341. [CrossRef]

29. Wu, Y.; Manthiram, A. Effect of surface modifications on the layered solid solution cathodes (1−z) Li[Li1/3Mn2/3]O2−(z) Li[Mn0.5−yNi0.5−yCo2y]O2. *Solid State Ionics* **2009**, *180*, 50–56. [CrossRef]

30. Liu, W.; Li, J.; Xu, H.; Li, J.; Qiu, X. Stabilized cobalt-free lithium-rich cathode materials with an artificial lithium fluoride coating. *Int. J. Miner. Met. Mater.* **2022**, *29*, 917–924. [CrossRef]

31. Chen, S.; Xie, Y.; Chen, W.; Chen, J.; Yang, W.; Zou, H.; Lin, Z. Enhanced Electrochemical Performance of Li-Rich Cathode Materials by Organic Fluorine Doping and Spinel Li$_{1+x}$Ni$_y$Mn$_{2-y}$O$_4$ Coating. *ACS Sustain. Chem. Eng.* **2019**, *8*, 121–128. [CrossRef]

32. Zhao, H.; Li, W.; Li, J.; Xu, H.; Zhang, C.; Li, J.; Han, C.; Li, Z.; Chu, M.; Qiu, X. Enhance performances of Co-free Li-rich cathode by eutesctic melting salt treatment. *Nano Energy* **2021**, *92*, 106760. [CrossRef]

33. Zhang, X.-D.; Shi, J.-L.; Liang, J.-Y.; Yin, Y.-X.; Zhang, J.-N.; Yu, X.-Q.; Guo, Y.-G. Suppressing Surface Lattice Oxygen Release of Li-Rich Cathode Materials via Heterostructured Spinel Li$_4$ Mn$_5$ O$_{12}$ Coating. *Adv. Mater.* **2018**, *30*, e1801751. [CrossRef]

34. Qiu, S.; Fang, T.; Zhu, Y.; Hua, J.; Chu, H.; Zou, Y.; Zeng, J.-L.; Xu, F.; Sun, L. Li1.2Mn0.6Ni0.2O2 with 3D porous rod-like hierarchical micro/nanostructure for high-performance cathode material. *J. Alloys Compd.* **2019**, *790*, 863–870. [CrossRef]

35. Zhou, L.; Tian, M.; Deng, Y.; Zheng, Q.; Xu, C.; Lin, D. La2O3-coated Li1.2Mn0.54Ni0.13Co0.13O2 as cathode materials with enhanced specific capacity and cycling stability for lithium-ion batteries. *Ceram. Int.* **2016**, *42*, 15623–15633. [CrossRef]

36. Gao, L.; Xu, Z.; Zhang, S. The co-doping effects of Zr and Co on structure and electrochemical properties of LiFePO4 cathode materials. *J. Alloys Compd.* **2018**, *739*, 529–535. [CrossRef]

37. Wang, L.; Wang, R.; Shi, Q.; Zhong, C.; Gong, D.; Lu, L.; Wang, X.; Liu, G.; Zhan, C. Enhanced high-voltage robustness of ultra-high nickel cathodes by constructing lithium-ion conductor buffer layer for highly stable lithium-ion batteries. *Appl. Surf. Sci.* **2022**, *605*, 154684. [CrossRef]

38. Hao, Y.-J.; Wang, Y.-Y.; Lai, Q.-Y.; Zhao, Y.; Chen, L.-M.; Ji, X.-Y. Study of capacitive properties for LT-Li4Mn5O12 in hybrid supercapacitor. *J. Solid State Electrochem.* **2008**, *13*, 905–912. [CrossRef]

39. Zheng, J.; Wu, X.; Yang, Y. A comparison of preparation method on the electrochemical performance of cathode material Li[Li0.2Mn0.54Ni0.13Co0.13]O2 for lithium ion battery. *Electrochim. Acta* **2011**, *56*, 3071–3078. [CrossRef]

40. Wen, L. Improved Electrochemical Performance of LaF3-coated Layered Oxide Li1.2Mn0.54Ni0.13Co0.13O2 Cathode Material for Lithium- Ion Batteries Prepared by Sol-Gel Method. *Int. J. Electrochem. Sci.* **2021**, *16*, 210344. [CrossRef]

41. Wu, F.; Lu, H.; Su, Y.; Li, N.; Bao, L.; Chen, S. Preparation and electrochemical performance of Li-rich layered cathode material, Li[Ni0.2Li0.2Mn0.6]O2, for lithium-ion batteries. *J. Appl. Electrochem.* **2009**, *40*, 783–789. [CrossRef]

42. Lu, C.; Wu, H.; Zhang, Y.; Liu, H.; Chen, B.; Wu, N.; Wang, S. Cerium fluoride coated layered oxide Li1.2Mn0.54Ni0.13Co0.13O2 as cathode materials with improved electrochemical performance for lithium ion batteries. *J. Power Sources* **2014**, *267*, 682–691. [CrossRef]

43. Yu, T.; Li, J.; Xu, G.; Li, J.; Ding, F.; Kang, F. Improved cycle performance of Li[Li0.2Mn0.54Co0.13Ni0.13]O2 by Ga doping for lithium ion battery cathode material. *Solid State Ionics* **2017**, *301*, 64–71. [CrossRef]

44. Liu, D.; Fan, X.; Li, Z.; Liu, T.; Sun, M.; Qian, C.; Ling, M.; Liu, Y.; Liang, C. A cation/anion co-doped Li1.12Na0.08Ni0.2Mn0.6O1.95F0.05 cathode for lithium ion batteries. *Nano Energy* **2019**, *58*, 786–796. [CrossRef]

45. Ma, Y.; Liu, P.; Xie, Q.; Zhang, G.; Zheng, H.; Cai, Y.; Li, Z.; Wang, L.; Zhu, Z.-Z.; Mai, L.; et al. Double-shell Li-rich layered oxide hollow microspheres with sandwich-like carbon@spinel@layered@spinel@carbon shells as high-rate lithium ion battery cathode. *Nano Energy* **2019**, *59*, 184–196. [CrossRef]

46. Zhang, Y.; Zhu, T.; Lin, L.; Yuan, M.; Li, H.; Sun, G.; Ma, S. Hierarchical Li1.2Mn0.54Ni0.13Co0.13O2 hollow spherical as cathode material for Li-ion battery. *J. Nanoparticle Res.* **2017**, *19*, 373. [CrossRef]

47. Chen, M.; Jiang, S.; Huang, C.; Xia, J.; Wang, X.; Xiang, K.; Zeng, P.; Zhang, Y.; Jamil, S. Synergetic Effects of Multifunctional Composites with More Efficient Polysulfide Immobilization and Ultrahigh Sulfur Content in Lithium–Sulfur Batteries. *ACS Appl. Mater. Interfaces* **2018**, *10*, 13562–13572. [CrossRef]

48. Zhang, J.; Yu, H.; Long, N.; Liu, T.; Cheng, X.; Zheng, R.; Zhu, H.; Ye, W.; Shu, J. Effect of calcination temperature on morphology and electrochemical performance of PbLi2Ti6O14. *Ceram. Int.* **2018**, *44*, 9506–9513. [CrossRef]

49. Vujković, M.; Stojković, I.; Cvjetićanin, N.; Mentus, S. Gel-combustion synthesis of LiFePO4/C composite with improved capacity retention in aerated aqueous electrolyte solution. *Electrochim. Acta* **2013**, *92*, 248–256. [CrossRef]